RSC Advances

PAPER

View Article Online
View Journal | View Issue

Cite this: *RSC Adv.*, 2019, **9**, 11170

Electro-deposition of bactericidal and corrosion-resistant hydroxyapatite nanoslabs†

Manisha Sharma,[ab] Rohit Nagar,[a] Vijay Kumar Meena*[ab] and Suman Singh *[ab]

Received 30th January 2019
Accepted 21st March 2019

DOI: 10.1039/c9ra00811j

rsc.li/rsc-advances

Herein, nanoscale hydroxyapatite (HA) with a slab-like morphology was synthesized, and its size was calculated to be in the range of 80–150 nm, as confirmed *via* scanning electron microscopy (SEM) and atomic force microscopy (AFM). The nanoscale HA with a slab-like structure has been referred as HA nanoslabs in the manuscript. The composition, crystallinity, wettability, bacterial resistance porosity, surface roughness and corrosion resistance of these HA nanoslabs were studied using energy dispersive spectroscopy (EDAX), X-ray diffraction (XRD), contact angle, colony count BET analyzer and profilometer and polarization techniques, respectively. The contact angle of the HA nanoslabs was found to be 22.6°, which indicated the hydrophilic nature of these nanoslabs. Their bacterial resistance was studied against the *Salmonella typhi* strain, and it was found that in the presence of the HA nanoslabs, the growth of the bacteria was hindered. For the corrosion resistance study, the HA nanoslabs were electro-deposited on a titanium alloy, used as a substrate. The deposition was carried out at varying currents, *viz*, 1 mA, 3 mA and 5 mA. The open circuit potential (OCP) and polarization were used for the estimation of the corrosion resistance of the bare and coated substrates. The corrosion potential started shifting towards noble potential, and the current density started decreasing with an increase in the electrochemical deposition current. This indicated good corrosion resistance of these nanoslabs.

1 Introduction

The market of orthopaedic devices is growing rapidly due to the improved economy, changed lifestyle and increased facility of health insurance. As orthopaedic devices, metal implants are being used for a long time to stabilize fractures, reduce pain or to restore joint functions. However, the success of an implant is highly dependent on some factors, such as its good biocompatibility, good mechanical properties *etc.* But generally, the implants fail due to infection or loosening caused by the corroded implant surface. This is mainly due to the fact that an implant is exposed to the hostile environment of living cells, tissues and biological fluids. This hostile environment makes the implant susceptible to localized corrosion in the human body or sometimes, the body considers it as a foreign entity and hence rejects it. In such cases, the surface modification of an implant material becomes important to reduce the chances of implant failure due to corrosion or infection.

Since about 50% of the bone is made up of the inorganic mineral hydroxyapatite (HA), HA is being widely used as a bone replacement material in a variety of orthopedic implants and artificial prostheses or as a coating material to promote bone growth inside the prosthetic implants. A number of methods, *viz*, thermal spraying, plasma spraying, ion-beam deposition, laser ablation and electrochemical deposition, have been reported for the coating of hydroxyapatite on implants.[1–5] Plasma spraying is the most commonly adopted technique for commercial HA coatings, however, it suffers from severe disadvantages such as poor adhesion, non-uniformity and possible degradation of hydroxyapatite due to the use of high temperatures during the coating process.[6] On the other hand, the thermal spraying method suffers from the disadvantages of poor coating, poor substrate adherence, and non-uniform crystallinity. High sintering temperatures used in thermal spraying can also result in crack propagation on the coating surface.[7] A review has been very well documented by Mohseni *et al.*, who very comprehensively analyzed nine different techniques used for hydroxyapatite coating.[8] Moreover, the advantages and disadvantages of these techniques were comprehensively discussed.

In recent years, due to the factors such as the requirement of low temperatures, the ability to control the coating thickness, the possibility to improve the substrate/coating bond strength using biocompatible linkers, the use of low cost equipment, the ease of experimentation, *etc.*, much interest has evolved in electrodeposition. The coating properties and surface structures can be easily controlled *via* electrochemical deposition technique just by changing the parameters such as applied potential and current density, deposition time, electrolyte temperature, ionic concentration and pH values.[9]

[a]*Central Scientific Instruments Organisation (CSIR-CSIO), Chandigarh, India. E-mail: ssingh@csio.res.in; vijaykumar@csio.res.in*

[b]*Academy of Scientific and Innovative Research (AcSIR-CSIO), Ghaziabad, India*

† Electronic supplementary information (ESI) available. See DOI: 10.1039/c9ra00811j

In this study, the synthesis of nanoslabs of hydroxyapatite and their electrochemical deposition on an implant material substrate, *i.e.* Ti_6Al_4V, using the currents of 1 mA, 3 mA, and 5 mA is reported. Before conducting the electrochemical deposition process, the shape, size, composition, crystallinity, wettability, bacterial resistance and corrosion resistance of the HA nanoslabs were well studied using scanning electron microscopy (SEM), atomic force microscopy (AFM), energy dispersive spectroscopy (EDAX), X-ray diffraction (XRD), contact angle, colony count and polarization techniques, respectively. After coating the implant substrate with the HA nanoslabs, the corrosion resistance of the substrate increased, as proved *via* the polarization studies.

2 Experimentation

2.1 Materials

Hank's solution, sodium hydroxide (NaOH), diammonium hydrogen orthophosphate $(NH_4)_2HPO_4$, *N*-cetyl-*N*,*N*,*N* trimethylammonium bromide ($C_{19}H_{42}BrN$), calcium chloride ($CaCl_2$), sodium chloride (NaCl), potassium phosphate dibasic (K_2HPO_4), ethanol (C_2H_5OH), nutrient agar, and nutrient broth were obtained from Sigma Aldrich, now owned by Merck.

2.2 Instrumentation

The Fourier transform infrared (FTIR) spectrum of the HA nanoslabs was obtained in the range of 400–4000 cm^{-1} using the Varian FTIR system (600 series, USA). The crystal structure of the nanoslabs was studied from their diffraction pattern, obtained using an X-ray diffractometer (XRD) from Bruker D8 Advance, Germany. The phase identification was achieved by comparing the sample diffraction pattern with the standard cards in the JCPDS database. The surface topology of the nanoslabs was observed by a field emission scanning electron microscope (FE-SEM), Model Quanta-200F coupled with an energy dispersive spectrometer, obtained from FEI, the Netherlands, which was used for elemental analysis. For the SEM studies, the samples were sputtered with gold for 60 s before imaging and examined at the accelerating voltage of 5 kV. The hydrophilicity of the HA nanoslabs was studied *via* the Kruss drop shape analysis system, Model DSA 100, using the sessile drop method. High-purity deionized water obtained *via* a Millipore water purifier was used for forming a drop on the surface to evaluate the wettability of the synthesized nanoslabs, and the measurements were conducted at room temperature. An atomic force microscopy (AFM) system, model XE-NSOM, Park Systems, Korea, was used for investigating the morphology and size distribution of the nanoslabs. The dynamic light scattering (DLS) studies were performed using a Zeta sizer obtained from Malvern. The surface area and porosity studies were performed on BET analyzer from Metrohm India Ltd., Model Belsorp Mini II. The pretreatment of samples was performed on Belprep-vac II analyzer. The electrodeposition and corrosion studies were performed using an electrochemical analyzer, Model CH1100, obtained from CHI instruments, USA. The corrosion studies of HA nanoslab-coated substrates were carried out using the Hank's solution as an electrolyte. The coated and uncoated Ti alloy was used as the working electrode, a platinum foil was used as an auxiliary electrode and Ag/AgCl was used as reference electrode. All studies were carried out at 37 °C. The surface roughness of the coated and uncoated implant material (Ti_6Al_4V) samples was measured using the Talysurf PGI 120 profilometer, where a Gaussian filter with a cut off of 0.8 mm was used. For bactericidal studies, incubation of the agar plates was conducted using a locally manufactured incubator. A gel doc system used for colony counting was obtained from Gold Sim, China. High-purity deionized water was used for the study, and the experiment was performed at room temperature.

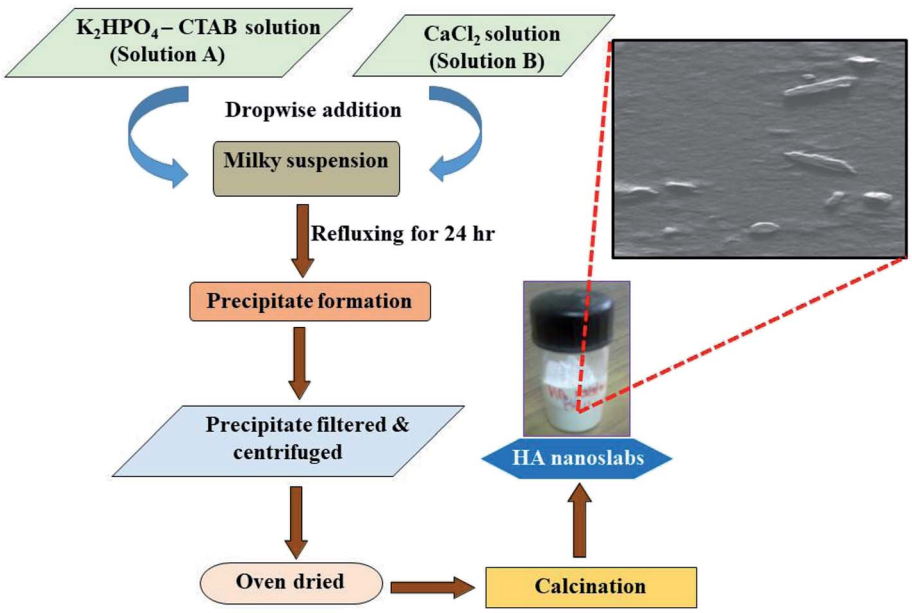

Fig. 1 A schematic showing the synthesis process for the HA nanoslabs.

2.3 Methodology

2.3.1 Synthesis of the hydroxyapatite nanoslabs. The synthesis of the hydroxyapatite nanoslabs was performed as reported in the literature[10,11] with some modifications. The procedure used for the synthesis is shown in Fig. 1. The complete protocol is mentioned in the ESI.† The porosity of the synthesized material was also studied and has been mentioned in the ESI.†

2.3.2 Electrodeposition of the HA nanoslabs. For electrodeposition, the HA nanoslabs were deposited on an implant material (a titanium alloy plate with 10 mm × 10 mm × 1 mm dimensions). Prior to electrodeposition, the titanium alloy substrate was polished with a silicon carbide (SiC) paper down to 220 grit. The substrate was washed with DI water to remove the residual grit and set for ultrasonic cleaning for 20 min in acetone and alcohol. A solution of the HA nanoslabs was prepared in a water and ethanol (1 : 1) mixture. Before electrodeposition, the solution was sonicated for 30 minutes to obtain a homogeneous suspension. The deposition was performed in three-electrode setup by applying the constant current of 1 mA, 3 mA, and 5 mA respectively. The setup consisted of the titanium plate as the working electrode, a platinum foil as the auxiliary electrode and Ag/AgCl as the reference electrode. The HA nanoslab suspension was stirred at a constant low stirring speed during the deposition process, and the pH of the solution was maintained at 6.5. The coated samples were sintered at 300 °C for 1 h under an inert atmosphere to increase the adhesion of the nanoslabs on the substrate.

2.3.3 Open circuit potential and corrosion studies. After electrodeposition of the HA nanoslabs on the substrate, open circuit potential (OCP) time measurements and corrosion studies were performed for bare and coated substrates with Hank's solution using the same three-electrode setup as mentioned above. In this case, the working electrode was the titanium alloy consisting of electrodeposited HA nanoslabs. The open-circuit potential (OCP) was measured for 400 s. For corrosion studies, potentiodynamic polarization curves *vs.* Ag/AgCl were obtained in the potential window from −0.2 V to −0.08 V at the scan rate of 50 mV s^{-1}. The corrosion potential and the corrosion current density were estimated by graphical extrapolation of the anodic and cathodic branches, which was automatically conducted in this case by a software associated with a potentiostat.

2.3.4 Bactericidal studies. For bactericidal studies, the MTCC-98 Sub-culture of *Salmonella typhi* was used, and a serial dilution method was adopted for the bacterial colony count experiment. Before initiating the experiments, all glassware was cleaned and autoclaved. After this, the nutrient agar and nutrient broth solutions were made by dissolving 2.8 g and 1.3 g of nutrient agar and nutrient broth, respectively, in 100 mL DI water in different flasks and autoclaved at 120 °C and 15 Pa for 15 min. After autoclaving, the agar solution was kept under a laminar air flow for some time for cooling, and then, agar plates were prepared. A sodium chloride solution was made by mixing 0.085 g of NaCl in 100 mL DI water. The solution was then autoclaved. Further, 9 mL of NaCl was placed in ten autoclaved bottles for serial dilution. This was followed by the addition of 1 mL of bacterial culture obtained from the nutrient broth culture to the first bottle, with the concentration 1×10^{-1} CFU. This mixture was serially diluted to the working concentration of 1×10^{-6} CFU. After the dilution process, 100 μL of the final diluted solution was spread on a nutrient agar plate. In another set, 1 mL solution of HA nanoslabs was mixed with the final diluted solution, and 100 μL of this mixture was spread on another nutrient agar plate. These plates were incubated in an incubator for 24 h at 37 °C. The colony counting was conducted *via* a gel-doc system.

3 Results and discussion

3.1 Mechanism of the HA nanoslab formation

The exact mechanism of the formation of the HA nanoslabs is not fully known, but it is based on the expected reaction; the plausible mechanism has been depicted in a schematic shown

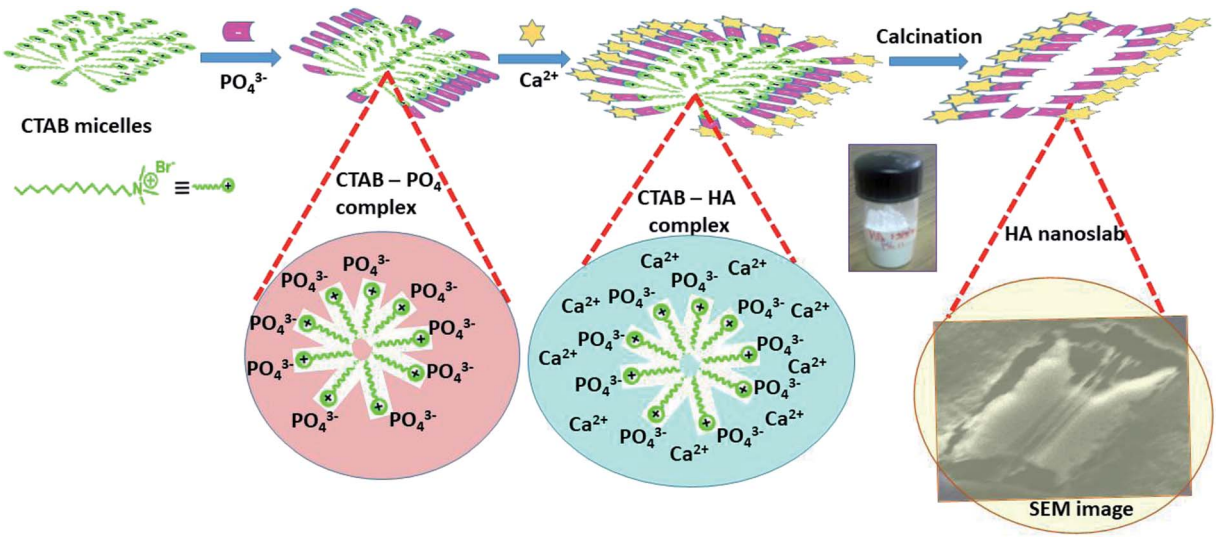

Fig. 2 Plausible mechanism of the HA nanoslab formation.

in Fig. 2. The main facilitator for the formation of slab-like hydroxyapatite is CTAB. When dipotassium phosphate is added to the CTAB solution, the negatively charged phosphate ions are attracted towards the surface of the CTAB micelles due to electrostatic attraction between them.[11] Both of them are stereo-chemically compatible to form a complex with each other due to their similar tetrahedral structure. The hexagonal complex micelle formed *via* the interaction of CTAB with phosphate ions might be acting as a nucleation center for the formation of hydroxyapatite.[12] After the addition of the calcium source, the particles get crystallized on the surface of the CTA–PO_4 micelle complex; thus, the CTA–HA complex is formed. After calcination of the CTA–HA complex, the surfactant gets removed, and a slab-like structure of hydroxyapatite is formed.

3.2 Characterization of the hydroxyapatite nanoslabs (HA nanoslabs)

3.2.1 Morphological and size-related characterization. The SEM image of the HA nanoslabs (Fig. 3(a)) shows the formation of a slab-like structure of hydroxyapatite having a size of about 80–150 nm. The EDS image shows the presence of calcium and phosphate elements (Fig. 3(b)) in HA. Fig. 3(c) and (d) show the 2D and 3D view of the atomic force microscopy image obtained for the HA nanoslabs, respectively. The AFM image also confirms the formation of slab-like structure of hydroxyapatite. Fig. 3(e) shows the size distribution obtained from the AFM image, and it indicates that the size of the HA nanoslabs is in the range from 80 to 120 nm. Fig. 3(f) shows the dynamic light scattering (DLS) results obtained for the nanoslabs of hydroxyapatite. The DLS result indicates that the size of the nanoslabs is 207 nm. In DLS, the size is calculated from the amount of light scattered by the particles. Analysis of the fluctuation of the scattered light thus yields information about the particles. However, this technique is not suitable for measuring the size of nanostructures having morphologies other than spherical as it considers the particles as spheres only. Moreover, DLS measures only the hydrodynamic radius of the sphere. The size calculated by the DLS technique is, therefore, always greater than the size determined *via* other techniques, such as TEM, SEM and AFM, as DLS also considers any adsorbed ions and solvent molecules during the size calculation.

3.2.2 Crystal structure study. X-ray diffraction analysis was employed to confirm the crystalline phase and the crystallite

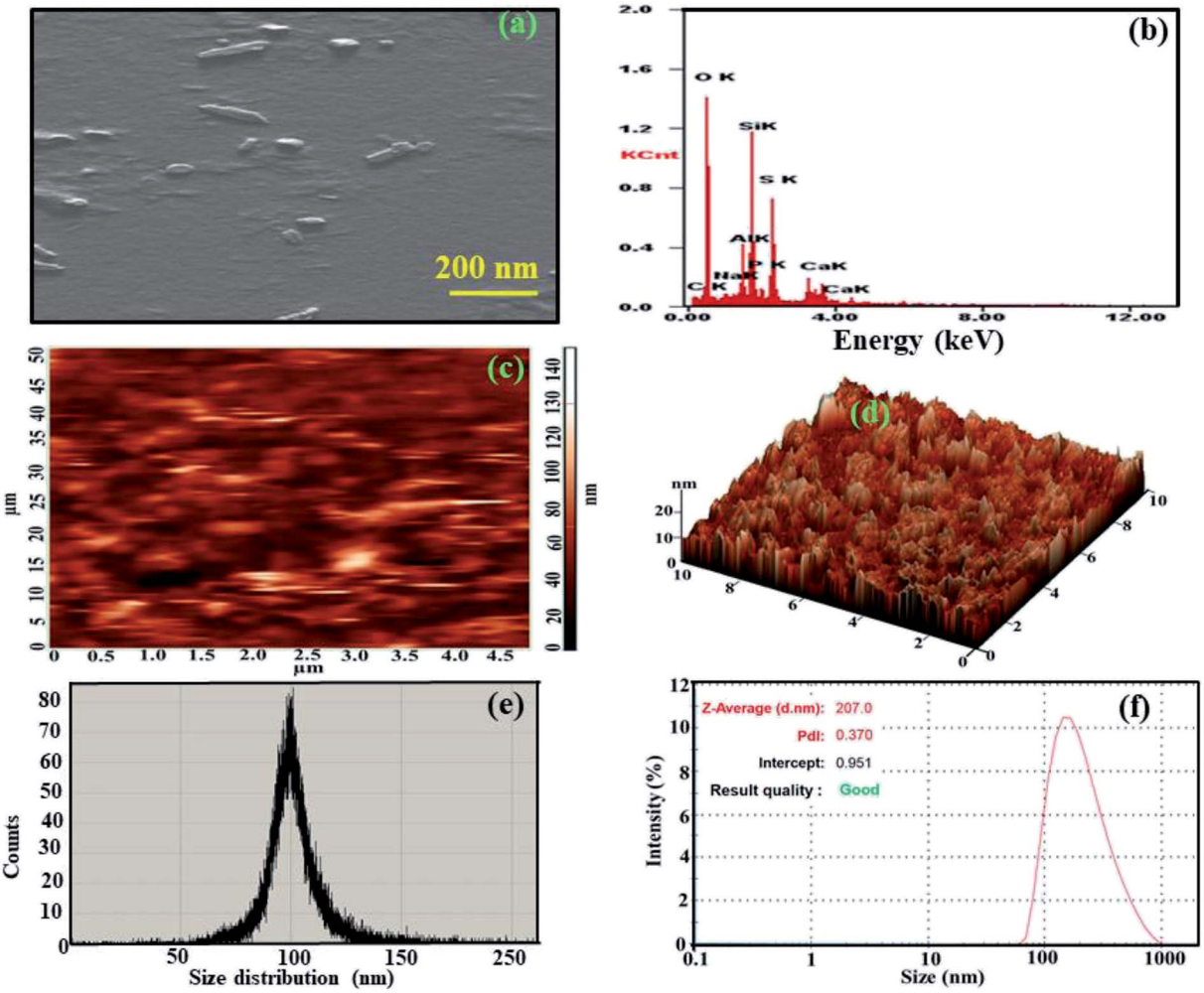

Fig. 3 (a) An FE-SEM image of the HA nanoslabs. (b) EDAX of the HA nanoslabs. (c) AFM image of the HA nanoslabs. (d) 3D AFM image of the HA nanoslabs. (e) Size distribution obtained from the AFM image of the HA nanoslabs. (f) DLS spectra of the HA nanoslabs.

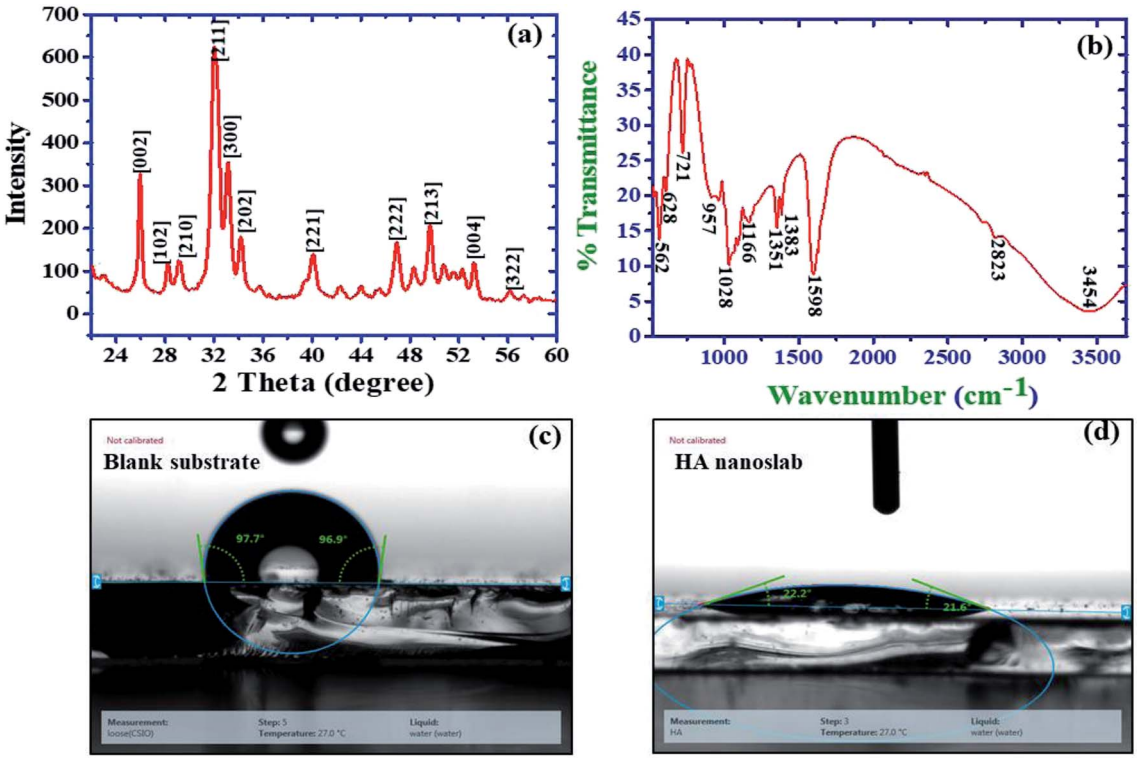

Fig. 4 (a) XRD pattern of the HA nanoslabs. (b) FTIR spectrum of the HA nanoslabs. (c) Contact angle of the blank substrate. (d) Contact angle of the HA nanoslab-coated substrate.

size of the powders. The results are shown in Fig. 4(a). The presence of wide XRD peaks can be attributed to the nanosize of hydroxyapatite and is an indication of the nanocrystalline nature of the synthesized powders. The main diffraction peaks were obtained at the 2θ values of 26, 28.16, 29.12, 31.9, 33.13, 34.02, 40.8, and 46.9 for the reflections of (002), (102), (210), (211), (300), (202), (221) and (222) planes, respectively. These peak positions are in good agreement with the JCPDS 09432 data. No peaks corresponding to other phases of calcium phosphate were obtained. The diffraction peaks and d spacing values are in coordination with the standard hexagonal structure and the $P6_3/m$ space group. The lattice parameters have the values $a = b = 0.940$ nm and $c = 0.615$ nm, which correspond to the JCPDS 9432 data. The broadening of the peaks can be related to the mean crystallite size using the Scherrer's equation:

Table 1 Parameters calculated from XRD of the hydroxyapatite nanoslabs

2θ	d (Å)	FWHM (°)	Plane	Crystallites (nm)
26.0	3.188	0.3	002	21.84
28.16	3.168	0.3	102	28.53
29.12	3.080	0.7	210	12.25
31.9	2.820	0.83	211	10.4
33.13	2.692	0.6	300	14.43
34.21	2.619	0.6	202	14.48
40.08	2.264	0.95	221	9.3
46.9	1.974	0.9	222	10.05

$$\beta(2\theta) = K\lambda/L \cos\theta$$

where L is the crystallite size, β is the full width half maximum, θ is the Bragg's angle, K is a constant and λ is the X-ray wavelength (1.54, CuKα radiation in our case). Using the above mentioned equation, the average crystallite size was found to be 15.18 nm. The crystallite size obtained from all the peaks is presented in Table 1.

The XRD data was also used to calculate the preference, which was used as a structure indicator. The preference is defined as the difference of RI from RIs:

$$P = (\mathrm{RI} - \mathrm{RIs})/\mathrm{RIs}$$

The relative intensity (RI) of the (002) peak as compared to that of the three strongest peaks for the standard powder HA sample (JCPDS 9432) is defined as $\mathrm{RI} = I_{(002)}/I_{(211)} + I_{(112)} + I_{(300)}$, where $I_{(002)}$, $I_{(211)}$, $I_{(112)}$, and $I_{(300)}$ are the intensities of the respective plane peaks. For the standard HA powder, the RI as calculated from JCPDS 9432 was found to be 0.182.[13] The calculated value for the preference growth for the 002 plane was 2.36. Zanin *et al.*[13] for their HA-graphene oxide composite found value of 2.61 for their preference growth along 022 plane.

3.2.3 Spectroscopic characterization. Fig. 4(b) shows the FTIR spectrum of the hydroxyapatite nanoslabs. The bands at 562 cm^{-1} and 628 cm^{-1} are derived from the ν_4 bending vibrations of the P–O mode, and the 960 cm^{-1} band has resulted from the presence of PO_4^{3-} ions (ν_1 symmetric P–O stretching vibrations).[14,15] The peak at 960 cm^{-1} is also an

indication of the crystalline nano-HA.[16] The strong band at 1028 cm^{-1} is also assigned to the P–O stretching vibrations of PO_4^{3-}. The peak at 1166 cm^{-1} indicates the ν_3 phosphate mode. The peaks at 1351 cm^{-1}, 1387 cm^{-1} and 1598 cm^{-1} are due to the presence of carbonate ions. The formation of carbonate might take place due to the adsorption of atmospheric carbon dioxide during ripening. The presence of the 1387 cm^{-1} band also indicated the partial substitution of traces of PO_4^{3-} by CO_3^{2-} to form a B-type carbon-substituted hydroxyapatite, which was similar to the apatite found in the bone.[17–19] The broad band at 3454 cm^{-1} is related to the absorbed water and OH^-. The band at 1387 cm^{-1} is the H–C bending mode, and the band at 721 cm^{-1} is the –(CH_2)– rocking mode, which may have originated from the CTAB moiety.

3.2.4 Contact angle measurements. Contact angle measurements were carried out to evaluate the wettability of HA nanoslabs. The contact angle indicates the wettability of the material surface, which in turn indicates the hydrophilic and/or hydrophobic characteristics of the material. In general, a hydrophobic surface possesses a contact angle above 90°, whereas a hydrophilic surface represents a contact angle value below 90°. The contact angle of HA nanoslabs is 22.6°, which indicates its hydrophilic nature (Fig. 4c and d). The hydrophilic surfaces are shown to promote the highest levels of cell attachment and proliferation.[20–23] Thus, the synthesized nanoslabs can be used to effectively coat the orthopedic implant materials.

3.2.5 Bacterial resistance study. Fig. 5(a–c) show the bactericidal study results obtained using the hydroxyapatite nanoslabs against *S. typhi*. The results show that as compared to the control, the nanoslabs are efficient in inhibiting the bacterial growth, as demonstrated by colony counting. In the control plate, about 20×10^7 CFU bacteria were found, whereas only 70×10^6 CFU bacteria were found in the plate with nanoslabs. If the concentration of the nanoslabs is optimized, they are believed to be quite effective as bactericidal agents.

3.2.6 Porosity and surface roughness studies. The porosity was determined for the synthesized samples of the HA nanoslabs using a BET analyzer. The total pore volume was found to be 0.2675 $cm^3\ g^{-1}$, calculated from the Barrett–Joyner–Halenda (BJH) plot, as shown in Fig. 5(d). The mean pore diameter of the HA nanoslabs is found to be 20.45 nm, which shows that the material is mesoporous in nature. In mesoporous materials, adsorption proceeds *via* multilayer adsorption followed by capillary condensation. This finally results in type IV and type V isotherms. The isotherm curves of the synthesized material are shown in Fig. 5(e). The figure shows a hysteresis loop, which is a characteristic feature of type IV isotherms, and this loop is associated with capillary condensation in mesopores. The steepness of the isotherm curves of the HA nanoslabs indicates the presence of aggregates of plate-like particles, giving rise to slit-like pores.[24] This also confirms the slab-like morphology of the HA nanoslabs. The mesoporous HA with pores of 2–50 nm can also be effectively used for drug release and drug storage applications.[25–27]

Surface roughness is one of the most important topographical parameters influencing the cell–material interaction. The surface roughness in the range from 10 nm to 10 μm may influence the interface biology since it is of the same order in size as that of small cells and large biomolecules. Keeping this in mind, the surface roughness was also monitored for the samples deposited at different currents *viz* 1 mA, 3 mA, and 5 mA. The achieved roughness of the substrates coated with nano-HA synthesized at 1 mA was 3.74×10^{-2} μm, which

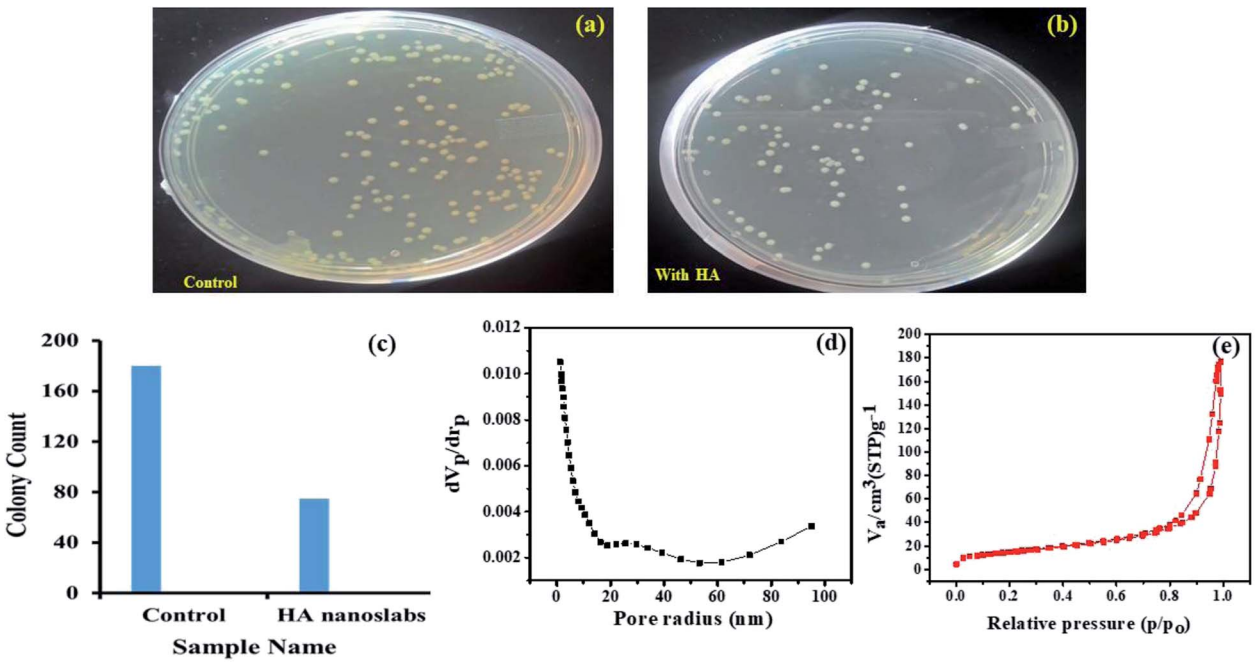

Fig. 5 Colony count: (a) control, (b) in the presence of the HA nanoslabs, (c) bar chart for colony count, (d) BJH pore size distribution curve, and (e) nitrogen adsorption–desorption isotherm curves.

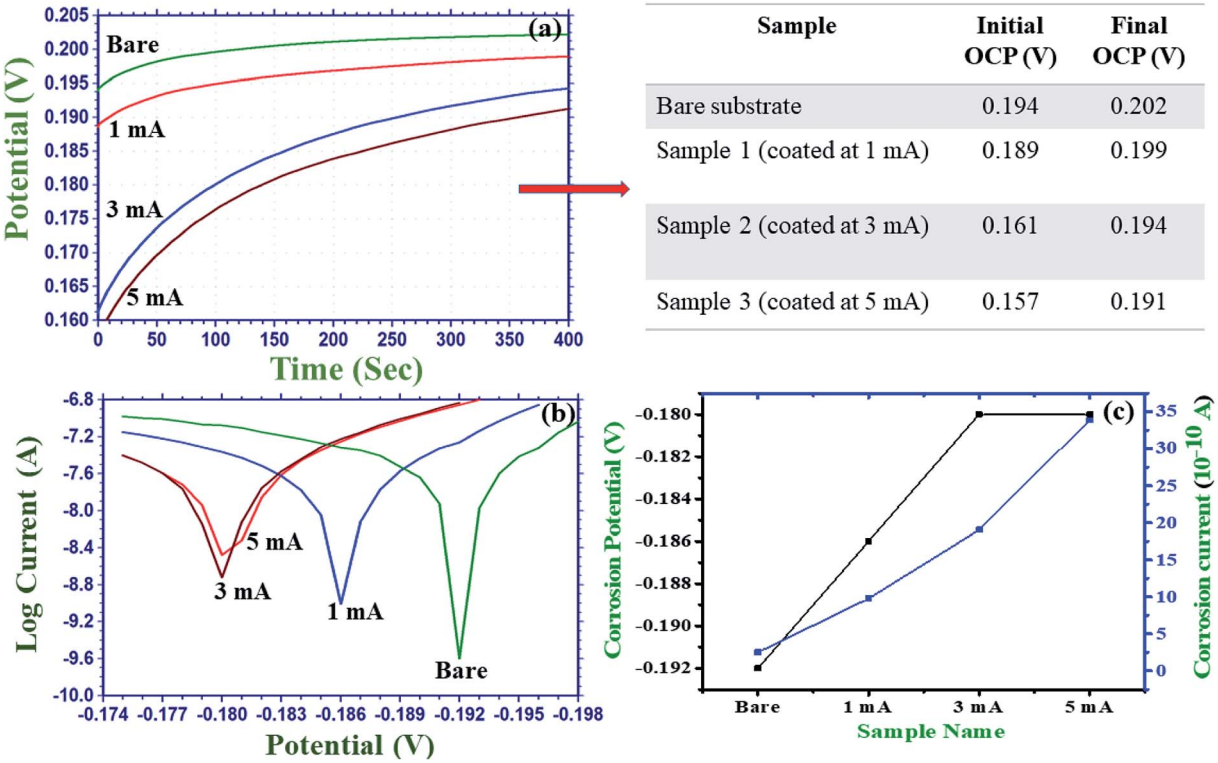

Sample	Initial OCP (V)	Final OCP (V)
Bare substrate	0.194	0.202
Sample 1 (coated at 1 mA)	0.189	0.199
Sample 2 (coated at 3 mA)	0.161	0.194
Sample 3 (coated at 5 mA)	0.157	0.191

Fig. 6 (a) Open circuit potential (OCP) obtained with the bare and the HA nanoslab-coated substrates and the respective values. (b) Polarization curves of the bare and coated substrates for the corrosion studies. (c) Change in the corrosion potential and corrosion current for different substrates.

continued to decrease as the deposition current increased. The surface roughness value reached 1.68×10^{-2} μm for 5 mA current density. For metals with the ability to form a passive layer, a decrease in the surface roughness increases the corrosion resistance.[28–30] This type of corrosion behavior has been reported for materials such as copper, nickel, aluminum, stainless steel, magnesium and titanium alloys. This concludes that the substrates electrolytically coated with HA at higher currents produced more corrosion resistive surfaces.

3.2.7 Electrochemical characterization

3.2.7.1 Open circuit potential study. Fig. 6(a) shows the open circuit potentials (OCP) obtained using the uncoated titanium alloy (bare substrate) and the coated substrates in the Hank's solution at room temperature. An OCP is the potential measured when no [net] current is flowing. As compared to that of the bare substrate, the OCP of the coated samples showed a shift towards the noble direction; this indicated the formation of an interface between the HA nanoslabs and the titanium alloy surface.[31] The initial OCP of the bare substrate was 0.194 V, which reached 0.202 V after about 250 seconds and remained constant for about 400 s. The associated table in Fig. 6(a) shows the values of the OCP obtained initially and after 400 s for the bare and the HA nanoslab-coated substrates. In all the cases, the initial OCP increased with time. The shift of the OCP towards noble behavior w.r.t time for the electrolytically coated substrates as compared to the case of the bare substrate can be due to the porous nature of hydroxyapatite. As a result, the electrolyte enters the coating through the pores.[31] From the values of the OCP, it is concluded that the HA nanoslabs deposited at the constant current of 5 mA are most robust in terms of corrosion resistance.

3.2.7.2 Corrosion studies. After being implanted in the body, the surface of an implant comes in contact with the biological fluids, interaction with which may involve changes in the local environment such as pH and ion concentrations. This leads to the loss of integrity. Therefore, the development of biomaterials that are resistant to corrosion is of prime importance. Herein, a corrosion resistant study was performed for the HA nanoslab-coated titanium alloy as the bioactivity and osteo-conductivity depend on the passivity of the coating. The corrosion mechanism involves two steps: the production of hydrogen ions (H^+) and the dissolution of HA in H^+ at high concentration. The production of hydrogen ions decreases the local pH at the sample–solution interface. This leads to high dissolution of the apatite coating.

Fig. 6(b and c) show the results obtained for the polarization curves, acquired using the uncoated and coated substrates. For the control substrate, bare titanium alloy was used. The figure showed that all the coated substrates showed better corrosion resistance as compared to the bare Ti_6Al_4V alloy substrate. The corrosion potential started shifting towards the noble potential, and the current density started decreasing in magnitude with an increase in the electrochemical deposition current. As is well-known, an electropositive corrosion potential and a low corrosion current density indicate good corrosion resistance. Therefore, this trend confirms the corrosion resistance behaviour of the coated substrates. The corrosion potential for the substrates

coated at 3 and 5 mA is, however, the same. These results are in agreement with those of the roughness and OCP studies.

4 Conclusion

The CTAB-mediated synthesis of nanoscaled hydroxyapatite resulted in the formation of a slab-like morphology with sharp edges, a plausible mechanism of which is discussed. The average size of the HA-nanoslabs was in the range of 80–150 nm. Hydroxyapatite finds its application in the biomedical domain, especially as a coating material for an implant surface. The coating material should be bacterial resistant as the rejection of an implant surface by the body may result in infection and thus in the loosening of an implant, and a revision surgery may be required. Moreover, the environment inside the body is full of fluids of various types. These fluids might cause corrosion of the implanted implant. Considering these facts, the motive of this study was to synthesize a bacterial- and corrosion-resistant material. The HA nanoslabs showed both bacterial and corrosion resistance. Researchers have used different combinations with hydroxyapatite to induce bacterial resistance; however, in this study, the HA nanoslabs themselves showed bacterial resistance. This might be due to the presence of CTAB during their synthesis or the sharp edges of the slab morphology. The exact mechanism needs to be explored.

Conflicts of interest

Authors don't have any conflict of interest.

Acknowledgements

Authors are thankful to the Director, CSIR-Central Scientific Instruments Organisation (CSIR-CSIO), for motivating us to carry out this research. M. S. also acknowledges the Department of Science and Technology (DST), New Delhi, for providing the SYST fellowship. Authors also acknowledge the help of M/s Metrohm India Limited, Chandigarh for extending their help for BET studies.

References

1 T. J. Levingstone, *et al.*, Plasma sprayed hydroxyapatite coatings: Understanding process relationships using design of experiment analysis, *Surf. Coat. Technol.*, 2015, **283**, 29–36.
2 J.-M. Choi, H.-E. Kim and I.-S. Lee, Ion-beam-assisted deposition (IBAD) of hydroxyapatite coating layer on Ti-based metal substrate, *Biomaterials*, 2000, **21**(5), 469–473.
3 P. Cheang and K. A. Khor, Thermal spraying of hydroxyapatite (HA) coatings: Effects of powder feedstock, *J. Mater. Process. Technol.*, 1995, **48**(1), 429–436.
4 G. Bolelli, *et al.*, Suspension thermal spraying of hydroxyapatite: Microstructure and in vitro behaviour, *Mater. Sci. Eng.*, 2014, **34**, 287–303.
5 M. Hamdi and A. Ide-Ektessabi, Preparation of hydroxyapatite layer by ion beam assisted simultaneous vapor deposition, *Surf. Coat. Technol.*, 2003, **163–164**, 362–367.
6 R. J. Talib and M. R. M. Toff, Plasma-sprayed coating of hydroxyapatite on metal implants–a review, *Med. J. Malays.*, 2004, **59**, 153–154.
7 C. M. Roome and C. D. Adam, Crystallite orientation and anisotropic strains in thermally sprayed hydroxyapatite coatings, *Biomaterials*, 1995, **16**(9), 691–696.
8 E. Mohseni, E. Zalnezhad and A. R. Bushroa, Comparative investigation on the adhesion of hydroxyapatite coating on Ti–6Al–4V implant: A review paper, *Int. J. Adhes. Adhes.*, 2014, **48**, 238–257.
9 A. Vladescu, *et al.*, Influence of the electrolyte's pH on the properties of electrochemically deposited hydroxyapatite coating on additively manufactured Ti64 alloy, *Sci. Rep.*, 2017, **7**(1), 16819.
10 J. M. Coelho, J. A. Moreira, A. Almeida and F. J. Monteiro, Synthesis and characterization of HAp nanorods from a cationic surfactant template method, *J. Mater. Sci.: Mater. Med.*, 2010, **21**(9), 2543–2549.
11 Y. Li, W. Tjandra and K. C. Tam, Synthesis and characterization of nanoporous hydroxyapatite using cationic surfactants as templates, *Mater. Res. Bull.*, 2008, **43**(8), 2318–2326.
12 G. Verma, K. C. Barick, N. Manoj, A. K. Sahu and P. A. Hassan, Rod-like micelle templated synthesis of porous hydroxyapatite, *Ceram. Int.*, 2013, **39**(8), 8995–9002.
13 H. Zanin, *et al.*, Fast preparation of nano-hydroxyapatite/superhydrophilic reduced graphene oxide composites for bioactive applications, *J. Mater. Chem. B*, 2013, **1**(38), 4947–4955.
14 Q. Li, *et al.*, In vitro synthesis of bioactive hydroxyapatite using sodium hyaluronate as a template, *J. Mater. Chem.*, 2012, **22**(38), 20257–20265.
15 M. C. Chang and J. Tanaka, FT-IR study for hydroxyapatite/collagen nanocomposite cross-linked by glutaraldehyde, *Biomaterials*, 2002, **23**(24), 4811–4818.
16 A. Antonakos, E. Liarokapis and T. Leventouri, Micro-Raman and FTIR studies of synthetic and natural apatites, *Biomaterials*, 2007, **28**(19), 3043–3054.
17 J. Ryu, *et al.*, Mussel-Inspired Polydopamine Coating as a Universal Route to Hydroxyapatite Crystallization, *Adv. Funct. Mater.*, 2010, **20**(13), 2132–2139.
18 C. Rey, *et al.*, The carbonate environment in bone mineral: A resolution-enhanced fourier transform infrared spectroscopy study, *Calcif. Tissue Int.*, 1989, **45**(3), 157–164.
19 Y. Deng, *et al.*, Biomimetic synthesis and biocompatibility evaluation of carbonated apatites template-mediated by heparin, *Mater. Sci. Eng.*, 2013, **33**(5), 2905–2913.
20 T. Ishizaki, N. Saito and O. Takai, Correlation of Cell Adhesive Behaviors on Superhydrophobic, Superhydrophilic, and Micropatterned Superhydrophobic/Superhydrophilic Surfaces to Their Surface Chemistry, *Langmuir*, 2010, **26**(11), 8147–8154.
21 D. P. Dowling, *et al.*, Effect of Surface Wettability and Topography on the Adhesion of Osteosarcoma Cells on

Plasma-modified Polystyrene, *J. Biomater. Appl.*, 2011, **26**(3), 327–347.

22 S. Irani, M. Zandi, N. Salamian, S. M. Saeed, M. D. Joupari and S. M. Atyabi, The study of P19 stem cell behavior on aligned oriented electrospun poly(lactic-co-glycolic acid) nano-fibers for neural tissue engineering, *Polym. Adv. Technol.*, 2014, **25**(5), 562–567.

23 C. Vasilescu, *et al.*, Characterisation and corrosion resistance of the electrodeposited hydroxyapatite and bovine serum albumin/hydroxyapatite films on Ti–6Al–4V–1Zr alloy surface, *Corros. Sci.*, 2011, **53**(3), 992–999.

24 K. S. W. Sing, D. H. Everett, R. A. W. Haul, L. Moscou, R. A. Pierotti, J. Rouquerol and T. Siemieniewska, Reporting physiorption data for gas/solid systems with Special Reference to the Determination of Surface Area and Porosity, *Pure Appl. Chem.*, 1985, **57**, 603–619.

25 C. K. Poh, *et al.*, In vitro characterizations of mesoporous hydroxyapatite as a controlled release delivery device for VEGF in orthopedic applications, *J. Biomed. Mater. Res., Part A*, 2012, **100**(11), 3143–3150.

26 G. F. Andrade, *et al.*, An in situ synthesis of mesoporous SBA-16/hydroxyapatite for ciprofloxacin release: in vitro stability and cytocompatibility studies, *J. Mater. Sci.: Mater. Med.*, 2014, **25**(11), 2527–2540.

27 X. Wu, *et al.*, Preparation of Mesoporous Nano-Hydroxyapatite Using a Surfactant Template Method for Protein Delivery, *J. Bionic Eng.*, 2012, **9**(2), 224–233.

28 M. Cabrini, A. Cigada, G. Rondell and B. Vicentini, Effect of different surface finishing and of hydroxyapatite coatings on passive and corrosion current of Ti6Al4V alloy in simulated physiological solution, *Biomaterials*, 1997, **18**(11), 783–787.

29 R. Walter and M. B. Kannan, Influence of surface roughness on the corrosion behaviour of magnesium alloy, *Mater. Des.*, 2011, **32**(4), 2350–2354.

30 R. B. Alvarez, H. J. Martin, M. F. Horstemeyer, M. Q. Chandler, N. Williams, P. T. Wang and A. Ruiz, Corrosion relationships as a function of time and surface roughness on a structural AE44 magnesium alloy, *Corros. Sci.*, 2010, **52**(5), 1635–1648.

31 S. G. Mohamed, A. A. Abdeltawab and M. A. Shoeib, Corrosion behaviour and bioactivity of electrophoretically deposited hydroxyapatite on titanium in physiological media (Hanks' solution), *Mater. Sci.*, 2012, **30**(3), 231–239.